



Two leading modes of the interannual variability in South American surface air temperature during austral winter

Yanjie Li¹ · Jianping Li^{2,3} · Fred Kucharski⁴ · Jin Feng⁵ · Sen Zhao^{6,7} · Jiayu Zheng⁸

Received: 29 May 2017 / Accepted: 6 November 2017 / Published online: 16 November 2017
© Springer-Verlag GmbH Germany, part of Springer Nature 2017

Abstract

The first two empirical orthogonal function (EOF) modes of the surface air temperature (SAT) interannual variability in the South American (SA) continent have been revealed in several previous studies. This presentation focuses on winter season and furtherly investigates the detailed advection and cloud-radiation processes and teleconnections from tropical sea surface temperature anomalies (SSTA) combining statistical analysis with Rossby wave dynamics and modelling experiments. The EOF1, featured with the anomalous center in the central part, is related to the tropical eastern Pacific SSTA, which may impact on the SA SAT variability through the Walker circulation and a regional Hadley cell. The anomalous center is largely attributed to low-level advection transported by the Hadley cell. The EOF2, as a fluctuation between anomalies in the southeast Brazil and the southern tip, is related to the SSTA surrounding the Maritime Continent, which may generate a barotropic wave train propagating to the SA continent. This wave train can strengthen high latitude westerly flow transporting warm advection to the southern tip, and generate southeast anomalous flow transporting cold advection to the southeast Brazil. Meanwhile, the cloud-radiation processes are also involved to enhance the advection-induced SAT anomalies in both areas.

Keywords Surface air temperature · Leading modes · South America · Temperature advection · Cloud-radiation effect

1 Introduction

The South American (SA) continent is flanked by the Atlantic and Pacific oceans, separated from the Antarctic Peninsula by the Drake Passage. It extends largely in the meridional direction, which results in diverse patterns of weather and climate over the continent (Garreaud et al.

2009). During austral winter (June–July–August, JJA), surface air temperature (SAT) ranges from 30 °C in the north to zero or below in the southernmost tip of the continent (figure not shown).

Many studies have revealed multiple temporal variability in the SA SAT. It is experiencing a warming climate (e.g. Vincent et al. 2005; Rusticucci 2012; Skansi et al. 2013;

✉ Jianping Li
ljp@bnu.edu.cn

¹ State Key Laboratory of Numerical Modeling for Atmospheric Sciences and Geophysical Fluid Dynamics, Institute of Atmospheric Physics, Chinese Academy of Sciences, Beijing, China

² State Key Laboratory of Earth Surface Processes and Resource Ecology and College of Global Change and Earth System Science, Beijing Normal University, Beijing 100875, China

³ Laboratory for Regional Oceanography and Numerical Modeling, Qingdao National Laboratory for Marine Science and Technology, Qingdao 266237, China

⁴ Earth System Physics Section, Abdus Salam International Centre for Theoretical Physics, Strada Costiera 11, Trieste 34151, Italy

⁵ Institute of Urban Meteorology, China Meteorological Administration, Beijing, China

⁶ School of Ocean and Earth Science and Technology, University of Hawaii at Mānoa, Honolulu, HI, USA

⁷ Key Laboratory of Meteorological Disaster of Ministry of Education, and College of Atmospheric Science, Nanjing University of Information Science and Technology, Nanjing, China

⁸ State Key Laboratory of Tropical Oceanography, South China Sea Institute of Oceanology, Chinese Academy of Sciences, Guangzhou, China

Torre and Marengo 2014). Torres and Marengo (2014) identified the winter mean SAT increasing as one of the climate change hotspots. The warming winter is thought to be related to the increasing global CO₂ emission. Collins et al. (2009) compared the differences in 2 m air temperature between the period 1948–1975 and 1976–2007. Northeast and central Brazil are found warmer in the recent period. Regarding the interannual variability, more studies have focused on the precipitation during the rainy season (e.g. Zhou and Lau 2001; Grimm and Natori 2006; Grimm and Zilli 2009; Grimm 2011) relative to the winter SAT.

However, the wintertime SAT exhibits remarkable yearly variability in the SA subregions. For example, Argentina experienced a cold winter with strong storms during July in 2007 (WMO 2008), while warm winters with heat waves in 2009 and 2013 (WMO 2010, 2014). Cold events in Argentina and even north to the southern Brazil are generally caused by the intrusion of polar outbreaks (e.g. Rusticucci and Vargas 1995; Schultz et al. 1998; Vera and Vigliarolo 2000), which can produce freezing conditions and reduce the agricultural production (e.g. Marengo et al. 1997; Marengo and Rogers 2001). Motivated by its enormous impact on the society and economy, observational and numerical studies have been done on cold surge cases (e.g. Marengo et al. 1997; Garreaud 1999; Vera and Vigliarolo 2000). Garreaud (2000) summarized the mean structure and dynamics of the cold air incursions over the subtropical SA region and their seasonal dependence. Müller and Berry (2007) pointed out the different large-scale circulation anomalies associated with more and less persistent generalized frosts. These studies suggest the seasonal mean background as an important modulator of the extreme cold events (Grimm 2011). Therefore, it is essential to study the yearly changes in the wintertime mean SAT.

Previous studies (e.g. Pittock 1980; Coronato and Bisigato 1998; Berman et al. 2013; Jacques-Coper and Bronnimann 2014) have examined seasonal mean SAT changes in the southeastern SA. Less discussed the whole SA continent. The interannual variability in SA climate is primarily impacted by El Niño–South Oscillation (ENSO) (e.g. Aceituno 1988; Kiladis and Diaz 1989; Halpert and Ropelewski 1992; Barros 2002; Grimm 2003, 2004), including the winter SAT (e.g. Barros et al. 2002). Recently, Kayano et al. (2017) examined the leading modes for all the four seasons in the whole SA continent, and emphasized the non-ENSO component, which is defined as the residual from the total SAT anomalies with the regressed part onto the Oceanic Niño Index removed. Therefore, there must be other impactors for the winter SAT variability in the SA continent besides ENSO. And this issue has not yet been explored in Kayano et al. (2017).

This work focus on the winter season and is organized as follow. Section 2 introduces the multiple used datasets,

preprocesses and methodologies. Dominant modes of the winter mean SAT interannual variability in the whole SA continent are compared with results in Kayano et al. (2017) in Sect. 3. Sequentially, associated temperature advection and cloud-radiation effects are discussed in several subregions. Besides, teleconnection from remote tropical sea surface temperature anomalies (SSTA) is also studied. Main findings are summarized and discussed in Sect. 4.

2 Data and methodology

2.1 Datasets

We use a monthly mean SAT dataset provided by the University of Delaware (Willmott and Matsuura 2001), available online at https://www.esrl.noaa.gov/psd/data/gridded/data.UDeI_AirT_Precip.html. The dataset has a horizontal resolution of $0.5^\circ \times 0.5^\circ$ and has been extensively used in land SAT variability studies (e.g. Garreaud et al. 2009; Jacques-Coper and Bronnimann 2014; Chen et al. 2016). The updated version 4 covers the period 1900/01–2014/12.

Circulation variables [including streamfunction, velocity potential, wind, sea level pressure (SLP), air temperature], total cloud cover, and radiation fluxes are from the National Centers for Environmental Prediction and the National Center for Atmospheric Research (NCEP/NCAR) reanalysis 1 (Kalnay et al. 1996). Streamfunction and velocity potential are computed from horizontal winds by the software NCAR Command Language (NCL). Circulation variables are on a regular 2.5° latitude–longitude grid. Total cloud cover and radiation fluxes are on T42 Gaussian grids. This dataset covers the period 1948/01 to present. Radiation fluxes are defined always positive (<https://www.esrl.noaa.gov/psd/data/gridded/flux.sign.ncep.html>).

The Precipitation Reconstruction (PREC) dataset provided by the National Oceanic & Atmospheric Administration (NOAA) from 1948/01 is used with values over both land and ocean (Chen et al. 2002). Sea surface temperature (SST) dataset is the NOAA Extended Reconstructed Sea Surface Temperature (ERSST) V4, which covers 1854/01 to present. The PREC data is on a $2.5^\circ \times 2.5^\circ$ grid, and ERSST on a $2^\circ \times 2^\circ$ grid.

All the above-mentioned datasets are used during the period 1948/01–2014/12. Considering the uncertainty in the quality of the cloud cover and radiation fluxes in NCEP/NCAR reanalysis before 1979, the monthly cloud cover data from ERA40 during the period 1958–2001 on the $1^\circ \times 1^\circ$ grid is also employed to support the analysis on the cloud-radiation effects. Results from both datasets are compared to suggest the consistence in this study. Details will be introduced in Sect. 3.

2.2 Preprocessing and statistical methods

The winter SAT averaged over the whole SA continent displays a significant warming trend (figure not shown). This trend is connected to global warming and has been detected in several subregions (e.g. Vincent et al. 2005; Rusticucci 2012; Skansi et al. 2013). To focus on the interannual variability, a 9-year high-pass Lanczos filter is applied to the monthly data on every grid and then the winter mean data is obtained with the first and last five years missed. We examined the percent of the SAT variance explained by the interannual component (which is defined as ratio of the standard deviation of the interannual component and the standard deviation of the SAT), which is above 70% in mostly regions. Similar preprocess on the SAT data is applied to discuss the interannual variability in the Eurasian continent during boreal spring (refer to Chen et al. 2016). All the other involved variables are high-pass filtered on the monthly data too.

Empirical orthogonal function (EOF) is used to examine the dominant modes of winter SAT variability in the SA continent. Similar results were obtained using rotated EOF (REOF, not shown). Simple linear regression of advection, radiation fluxes and circulation variables are developed onto the normalized PCs, which denote anomalies in these fields corresponding to one PC's standard deviation. Multiple linear regression is applied to quantify the separate contributions of advection and radiation to the SAT variability in several regions. Correlation analysis is employed to discuss the relationship between the EOFs and the global SSTA.

2.3 Diagnosis of Rossby wave dynamics

In this work, the diagnosis of Rossby wave dynamics considers the Rossby wave sources (RWS) and propagation paths. It is difficult to exactly quantify the RWS, since complex adiabatic forcing can disturb the free atmosphere. Sardeshmukh and Hoskins (1988) proposed that divergent winds induced by strong tropical heating can transport the relative vorticity to the extratropics as a kind of RWS. The theoretical model is the vorticity equation

$$\frac{\partial \xi}{\partial t} + u_{\psi} \frac{\partial \xi}{\partial x} + v_{\psi} \frac{\partial \xi}{\partial y} = RWS + F, \quad (1)$$

where ξ is the relative vorticity; (u_{ψ}, v_{ψ}) are the rotational wind components; x and y are longitude and latitude, respectively; and F is the frictional term. RWS is defined as

$$RWS = -u_x \frac{\partial \xi}{\partial x} - v_x \frac{\partial \xi}{\partial y} - \xi D, \quad (2)$$

where u_x, v_x are the divergent wind components and D is the divergence.

Two-dimensional Rossby wave propagation is an important pathway for the large-scale atmospheric responses to remote forcing. It can be depicted by the Rossby wave ray tracing trajectory, following Hoskins and Karoly (1981). Limited by the linear perturbation decomposition, the wave ray trajectory is dependent on the fixed basic state. Starting from (1) and ignoring terms on the right, the wave ray equations can be derived based on the horizontally non-uniform basic state (such as the climatological flow) under the WKB approximation (e.g., Karoly 1983; Li and Nathan 1997; Li and Li 2012; Li et al. 2015; Zhao et al. 2015). In this study, the basic state is fixed as the climatological JJA low-frequency flow (i.e., after the 9-year low pass filter). This flow is two-dimensionally smoothed to remove small scale disturbances. The initial zonal wavenumber is set to 3. Details on the wave ray theory and calculation can be found in Li et al. (2015) and Zhao et al. (2015).

2.4 Atmospheric general circulation model (AGCM)

The Simplified Parameterizations, Primitive Equation Dynamics (SPEEDY) model (Molteni 2003; Kucharski et al. 2006, 2013), developed at the Abdus Salam International Centre for Theoretical Physics, Trieste, Italy, is used to perform idealized numerical experiments to verify the linear atmospheric responses to tropical SSTA. SPEEDY is an intermediate-complexity AGCM based on a spectral primitive-equation dynamical core (Held and Suarez 1994). It is run with a spectral truncation at a total wavenumber 30, on a 96×48 global grid (resolution of $\sim 3.8^\circ$ in latitude and longitude), with eight vertical levels. Information on this model can be found at <http://www.ictp.it/~kucharsk/speedy-net.html>.

The SPEEDY model has been used effectively in many climate studies to investigate ENSO teleconnections (e.g. Bracco et al. 2004; Heger-Bulic and Brancovic 2007; Kucharski et al. 2007; Yadav et al. 2010; Dogar et al. 2017), tropical Atlantic teleconnections (e.g. Kucharski et al. 2009, 2011; Rodriguez-Fonseca et al. 2009; Losada et al. 2012; Nnamchi et al. 2013; Sun et al. 2015; Mohino and Losada 2015), and the SA monsoon and circulations (Barreiro and Tippmann 2008; Zamboni et al. 2012).

3 Results

3.1 Two leading EOF modes

Figure 1 shows the spatial distribution of the first (EOF1) and second (EOF2) modes for the winter SA SAT anomalies and their corresponding PCs. EOFs and PCs shown here

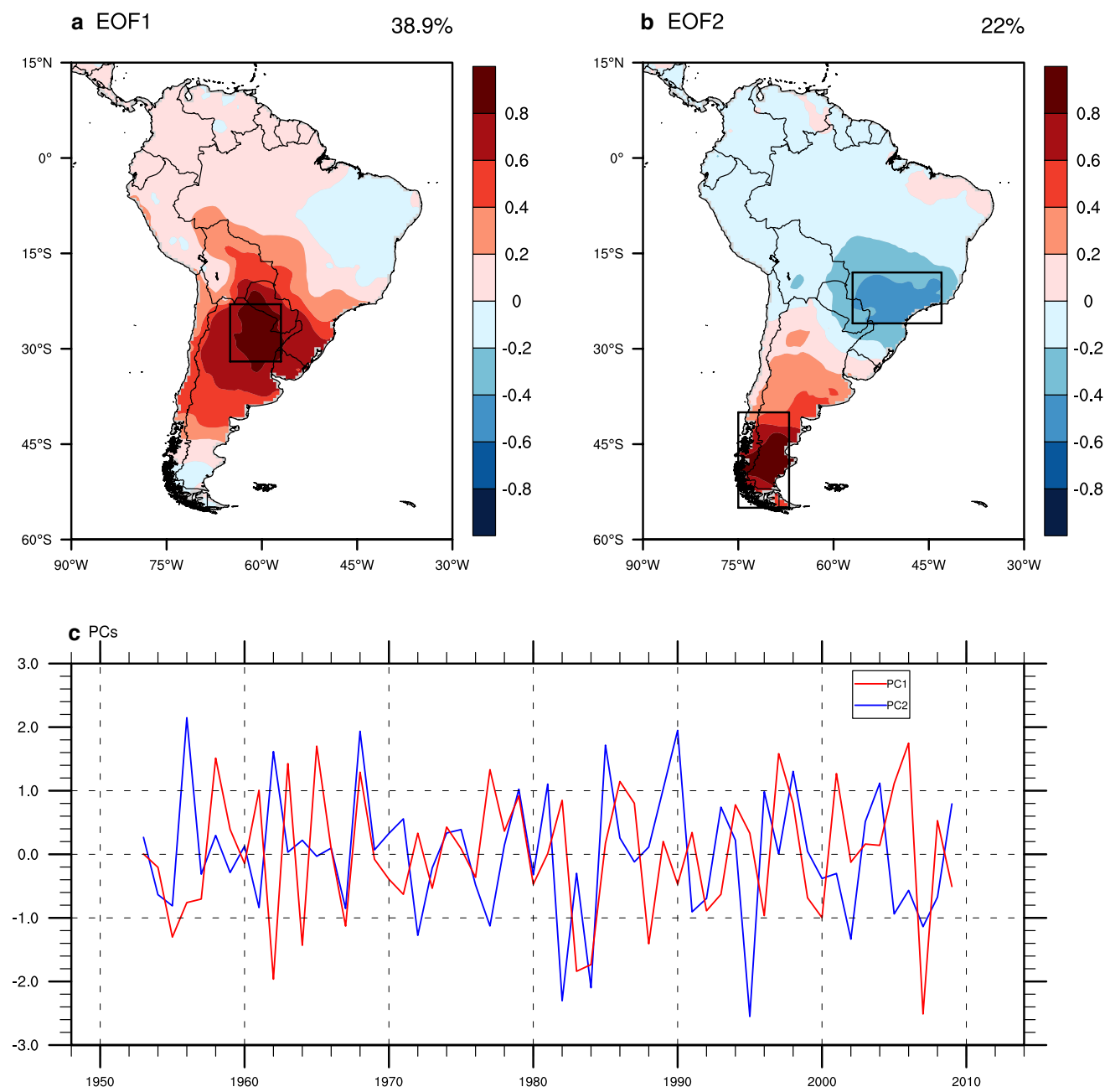


Fig. 1 The EOF1 and EOF2 of the austral winter SAT interannual variability in the South America (unit: °C), based on 9-year high-pass filtered monthly dataset covering 194801–201412 and the corresponding normalized PCs. EOFs are multiplied by the standard deviation of the corresponding PCs (27.8 °C and 20.9 °C respectively). The EOF1 and EOF2 explain 38.9% and 22% variances of the

total. Since the data are filtered to keep the interannual signal with a period less than 9 years, values in the first and last 5 years are missing. Black rectangulars denote the areas with significant SAT anomalies, the central region (32°S–23°S, 295°E–303°E) in **a**, southeast Brazil (26°S–18°S, 303°E–317°E) and the southern tip (55°S–40°S, 285°E–293°E) in **b**

are standardized to identify their abnormal years (Storch and Zwiers 2003). The EOF1 and EOF2 can explain 38.9 and 22% of the variances respectively. These two modes are well separated based on the method of North et al. (1982).

The EOF1 mode is characterized by significant anomalies in the central part, especially Paraguay and northern

Argentina. This region experiences warmer than normal conditions in the years 1958, 1961, 1963, 1965, 1968, 1977, 1986, 1997, 2001, 2005, and 2006 (with positive PC1 greater than 1 standard deviation, listed in Table 1), and cooler than normal conditions in the years 1955, 1962,

Table 1 List of years with positive PCs higher than 1 and negative PCs lower than -1

	PC1	PC2
Positive	1958, 1961, 1963, 1965, 1968, 1977, 1986, 1997, 2001, 2005, 2006 (11)	1956, 1962, 1968, 1979, 1981, 1985, 1989, 1990, 1998, 2004 (10)
Negative	1955, 1962, 1964, 1967, 1983, 1984, 1988, 2007 (8)	1972, 1977, 1982, 1984, 1995, 2002, 2007 (7)

1964, 1967, 1983, 1984, 1988, and 2007 (with negative PC1 less than -1 standard deviation, listed in Table 1).

The EOF2 mode exhibits a north-south dipole pattern. A warmer south-cooler north pattern occurs in the years 1956, 1962, 1968, 1979, 1981, 1985, 1989, 1990, 1998, 2004 (with positive PC2 greater than 1 standard deviation, listed in Table 1). An opposite pattern occurs in the years 1972, 1977, 1982, 1984, 1995, 2002, 2007 (with negative PC2 less than -1 standard deviation, listed in Table 1). Anomalies are particularly remarkable in the southernmost portion of the continent and the southeast Brazil. The north-south dipole SAT pattern in the southeastern SA has been reported previously (Pittock 1980; Coronato and Bisigato 1998; Berman et al. 2013). Here, the EOF2 pattern for the whole SA continent further confirms the SAT fluctuation in an extensive range.

Dominant characteristics of these two EOF modes reproduce the Fig. 3 in Kayano et al. (2017). Differently, the long-term SAT trend is removed for every grid in their work. The explained variances by the EOF1 and EOF2 in their study are 31.1 and 17.2%, both smaller than the results in this study. It reasons from the multidecadal and decadal variations remained in the detrended SAT data as they discussed in their conclusion section. Additionally, spectrum analysis on the PCs in this study reveals the maximum peak of the spectral power appears at the 2-4-year period (figure not shown). These information suggests the high-pass filter as an effective tool in reflecting the interannual variability.

3.2 Physical processes

Multiple physical mechanisms, such as the rainfall-cloud-radiation, albedo-radiation, and temperature advection processes, may affect SAT changes. Dominant physical processes vary with the land surface covering and local tropospheric circulations in different regions. For the SA SAT, temperature advection by low-level winds and precipitation are examined as contributors (Barros et al. 2002; Kayano et al. 2017), but Fig. 5a and b in Kayano et al. (2017) do not suggest the precipitation as a robust factor in the spatial characteristics of the winter SAT modes. We here attempt to examine the associated advection and cloud-radiation terms with the two EOF modes.

The temperature advection process, in a linearized framework, can be decomposed into four terms: $-u' \frac{\partial \bar{T}}{\partial x}$, $-v' \frac{\partial \bar{T}}{\partial y}$, $-\bar{u} \frac{\partial T'}{\partial x}$, $-\bar{v} \frac{\partial T'}{\partial y}$. Sum of the first two terms

$\left(-u' \frac{\partial \bar{T}}{\partial x} - v' \frac{\partial \bar{T}}{\partial y}\right)$ denotes the advection of the climatological temperature by the wind anomalies. Sum of the last two terms denotes the advection of the anomalous temperature by the climatological wind. Sum of the four terms denotes the total advection effect. These quantities are calculated at 850 hPa and then regressed onto the normalized PC1 and PC2.

The effect of the cloud on the radiation fluxes and SAT are complicate. On the one hand, cloud cover can reduce incoming shortwave radiation (SWR), resulting in a cooling SAT anomaly. On the other hand, it can reflect outgoing longwave radiation (LWR) back to the surface, resulting in a warming SAT anomaly. These are direct effects of the cloud on the SAT, and the indirect effects are beyond our study and not discussed. Combining with Figs. 2, 3 and 4, we will analyze the advection and cloud-radiation effects associated with the two EOFs for the SA subregions. In Figs. 3 and 4, positive upward fluxes represent heat loss by the surface, positive downward fluxes represent heat gained by the surface. Positive net fluxes represent the upward component greater than the downward component, i.e. heat loss by the surface.

Corresponding to the remarkable warm center in the positive EOF1 (indicated as the black rectangular in Fig. 2a-c), warm advection of the climatological temperature by the northerly wind anomaly from the Amazon region is observed significantly. Meanwhile in the southeast Patagonia, there is totally cold advection to the east of Andes (Fig. 2a, b). It mainly arises from the term $-v' \frac{\partial \bar{T}}{\partial y}$ (meridional advection of

the climatological temperature, included in Fig. 2b) and that the meridional wind anomalies are more significant than the zonal wind component (see the arrows in Fig. 2b). Contrary to the cold advection, the SAT associated with the positive EOF1 becomes warm at the latitudes 45°S-30°S, which indicates other processes are more relevant as discussed later. Gurreaud (2000) studied the important role of the Andes Mountain as a topographic block to generate ageographic flow in the cold air intrusion into the low-latitudes. This effect seems active at the latitudes north of 40°S, which may relate to the significant cold advection observed in the Fig. 2c. Two cold advection surges extend from the Andes at about the latitude 30°S, one northeast into the tropics and the other one covering the central Patagonia.

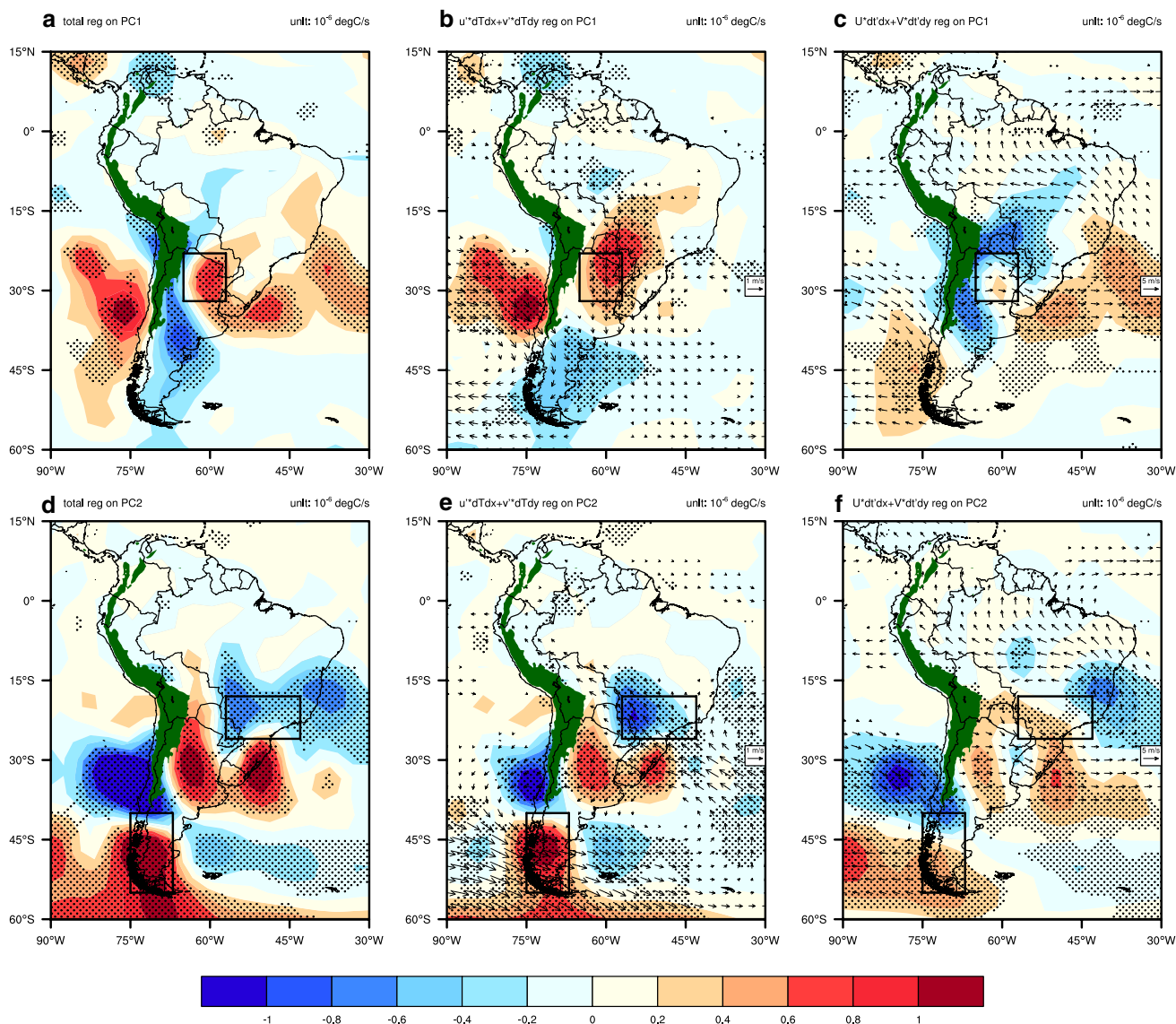


Fig. 2 Associated linear advection anomalies (unit: $10^{-6} \text{ }^{\circ}\text{C s}^{-1}$) at 850 hPa by regressed onto the normalized PCs. **b**, **e** Show advection by wind anomalies, **c**, **f** advection by climatological wind, **a**, **d** their sum. Arrows in **b** and **e** (unit: m s^{-1}) denote the wind anomalies regressed on PCs, with magnitude greater than 0.5 m s^{-1} . Arrows

in **c** and **f** denote the JJA climatological wind based on the filtered monthly data, with magnitude greater than 1 m s^{-1} . Dark green shading indicates the topography above 1500 m. Stippling indicates anomalies significantly away from zero at the 90% confidence level according to the two-tailed Student's *t* test

In the southern SA region between latitudes 45°S – 30°S , the cloud cover increases up to 2% when the normalized PC1 positively changes one standard deviation. Correspondingly, both the upward and downward SWR decreases, and the net SWR displays positive anomalies due to the larger downward component in magnitude (Fig. 3b, e, f). Oppositely, the upward LWR increases with the warm SAT, and the downward LWR increases as a result of the increased upward component and the increased cloud cover (Fig. 3g, h). The net LWR displays negative anomalies due to the larger downward component in magnitude (Fig. 3c). Although the SWR and LWR fluxes offset each other, the net fluxes exhibit

totally negative anomalies, which are significant at the 90% confidence level by the student's *t*-test (Fig. 3d). Therefore, the sum effect of these cloud and radiation fluxes anomalies favor warm SAT anomalies in this region, which is opposite to the cold condition due to the advection effect as above discussed. Similarly, the northern SA in the north of 5°S experiences cold advection anomalies and decreased cloud cover. The latter corresponds to the increased downward SWR in favor of warming this region (Fig. 3a, f). This opposite effect of the advection and radiation is possibly reasoning for the non-significant SAT anomalies in these regions (see Fig. 1a).

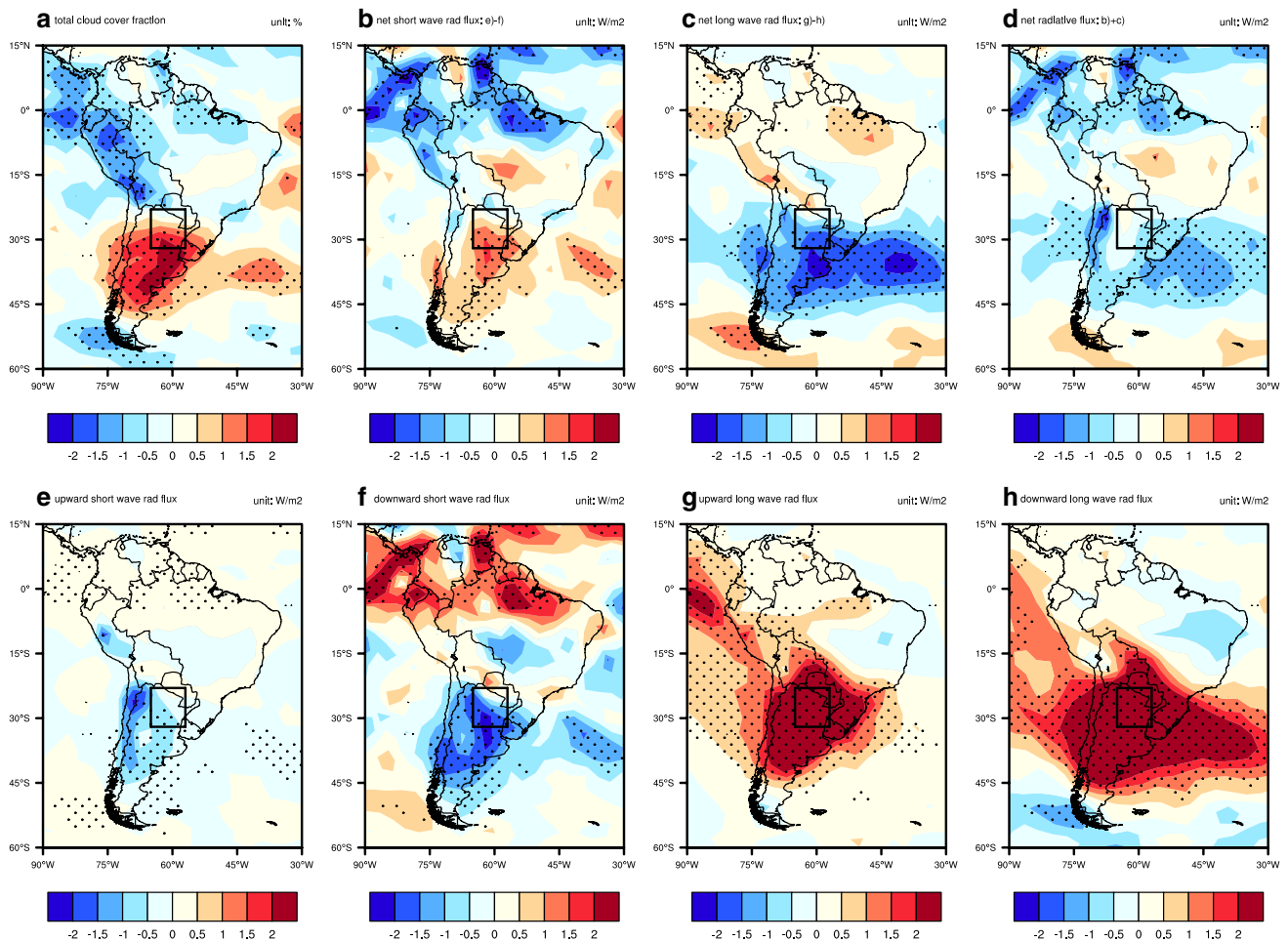


Fig. 3 Anomalies in **a** total cloud cover (unit: %), **b** net shortwave radiation flux (unit: W m^{-2}), **c** net longwave radiation flux (unit: W m^{-2}), **d** the sum of the net long and shortwave radiation flux (unit: W m^{-2}), **e** upward shortwave radiation flux (unit: W m^{-2}), **f** downward shortwave radiation flux (unit: W m^{-2}), **g** upward longwave radiation flux (unit: W m^{-2}), and **h** downward longwave radiation flux (unit: W m^{-2}) by regressed onto the normalized PC1. Positive upward fluxes

represent heat loss by the surface, positive downward fluxes represent heat gained by the surface. Positive net fluxes represent the upward component greater than the downward component, i.e. heat loss by the surface. Stippling indicates anomalies significantly away from zero at the 90% confidence level according to the two-tailed Student's *t*-test. Black rectangular is defined in Fig. 1a

Associated with the EOF2, anomalies in temperature advection at 850 hPa are shown as Fig. 2d–f. Significant cold advection is observed in the southeast Brazil, corresponding to the cold SAT anomalies here. Meanwhile, significant warm advection is observed in the continent's southern tip, where display warm SAT anomalies. It suggests that the north–south dipolar pattern in SAT is related to the opposite advection anomalies in the two polar regions.

Figure 4 shows anomalous signals in total cloud cover, SWR and LWR associated with the EOF2. Significant decreasing and increasing cloud cover anomalies are observed in the southeast Brazil and the southern tip, respectively. Corresponding to the less cloud cover, more downward SWR is found in the southeast Brazil. At the same time, the upward LWR is reduced with the cold SAT

anomalies in this region, and the downward LWR is reduced more significantly in the magnitude. The total of these components is determined by the downward LWR. Therefore, the net cloud-radiation effect favors cold SAT anomalies in the southeast Brazil. Similarly, we can analyze that the net cloud-radiation effect favors warm anomalies in the southern tip by increasing downward LWR back to the surface.

As a summary of the above qualitative discussion, both the advection and cloud-radiation effects are associated with the EOFs. They offset each other sometimes resulting in weak SAT changes, for example, at the subtropical latitudes 45°S–30°S and tropical region north of 5°S for the EOF1. While sometimes, they play the same effect on the SAT resulting in strong SAT changes, for example, in the regions: the central part (32°S–23°S, 295°E–303°E) in

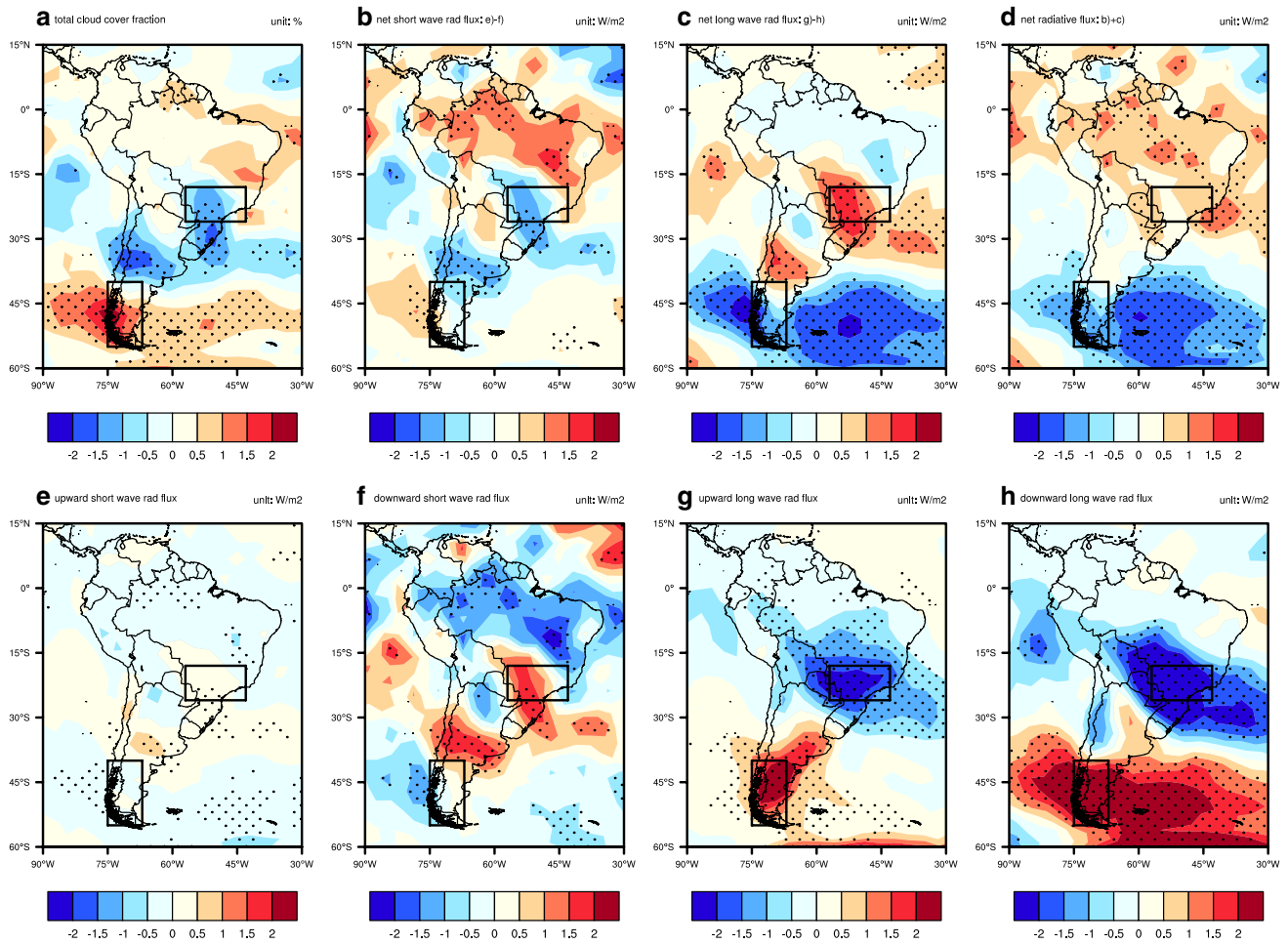


Fig. 4 Same as the Fig. 3, but regressed onto the normalized PC2. Black rectangulars are defined in Fig. 1b

EOF1, the southeast Brazil (26°S–18°S, 303°E–317°E) and the southern tip (55°S–40°S, 285°E–293°E) in EOF2. These regions are denoted as the black boxes in the Fig. 1.

To quantitatively understand their contributions to the SAT changes, we employ the multiple linear regression model to fit the normalized PC1 and PC2. Advection terms by wind anomalies $\left(-u' \frac{\partial \bar{T}}{\partial x} - v' \frac{\partial \bar{T}}{\partial y}\right)$, advection terms by climatological wind $\left(-\bar{u} \frac{\partial T'}{\partial x} - \bar{v} \frac{\partial T'}{\partial y}\right)$, and net radiation flux are averaged over the defined three regions and normalized. For the PC1, the factors from the central part are used to establish the model. For PC2, the factors from the southeast Brazil and the southern tip are used respectively. These three models can fit the corresponding PCs significantly by the F test. The partial regression coefficients suggest the advection by wind anomalies is the primary contributor for the PC1 variability in the central region and for the PC2 in the southeast Brazil. Its weights are twice the net radiation flux in both situations. In the southern tip, both the advection by

wind anomalies and radiation are dominant factors for the PC2. The latter is weighted 1.5 times greater than the former.

3.3 Atmospheric circulation changes and dynamics

3.3.1 Upper and lower tropospheric circulations

Previous results suggest that the wind-induced advection and the cloud-radiation effect are important factors in controlling SAT variability in the SA continent. These two factors are closely related to the atmospheric circulation. The associated circulation anomalies corresponding to the EOF1 and EOF2 will be analyzed in this section. Figure 5 shows the global streamfunction anomalies at 200 hPa and 500 hPa, and SLP anomalies associated with the EOF1 and EOF2 by regression upon the corresponding normalized PCs. The zonal mean of both the streamfunction and SLP is removed. Associated wind anomalies at different altitudes are shown as vectors.

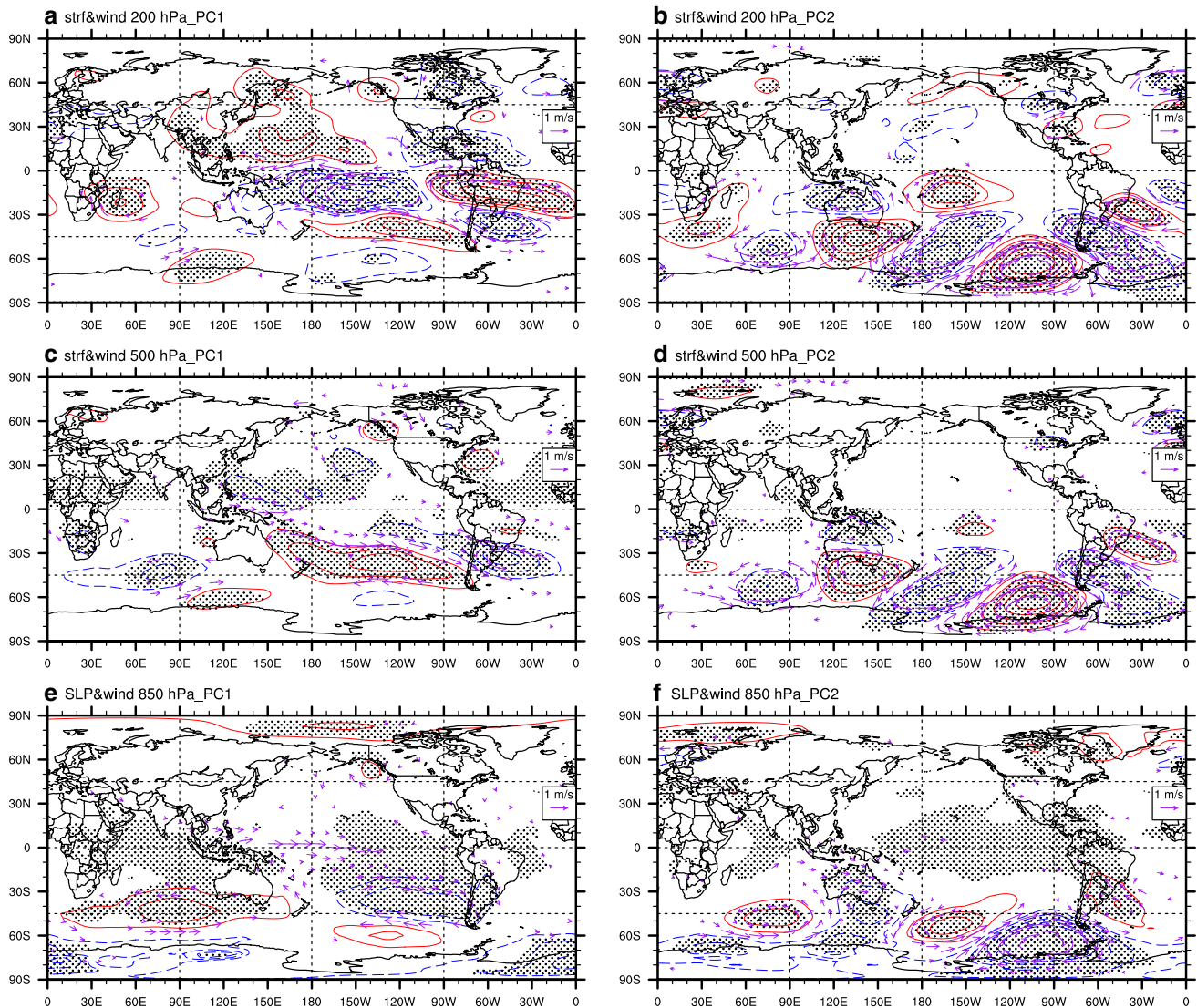


Fig. 5 Circulation anomalies regressed onto the normalized PC1 (left panels) and PC2 (right panels). **a, b** show the eddy streamfunction (contour, unit: $10^6 \text{ m}^2 \text{ s}^{-1}$) and wind (vector, unit: m s^{-1}) at 200 hPa, **c, d** are the same as **a** and **b**, but for 500 hPa. **e, f** show the zonal departure of sea level pressure (contour, unit: mb) and 850 hPa wind (vector, unit: m s^{-1}). Contours are shown from -2 to 2 with an inter-

val of 0.1 . Negative contours are blue, positive are red. Stippling indicates contours significantly away from zero at 90% confidence level according to the two-tailed Student's *t*-test. Wind vectors are shown over the regions where either component of the wind anomalies is significantly different from zero at the 90% confidence level according to the two-tailed Student's test

Corresponding to the EOF1 mode, the tropospheric streamfunction anomalies display a baroclinic–barotropic coupled pattern (Fig. 5a, c, e). A baroclinic Gill-type quadrupole (with one pair of positive and negative streamfunction centers over the Pacific, and one pair over the Americas) appears at tropics in the upper troposphere, but disappears at lower levels. The extratropical streamfunction anomalies display a quasi-barotropic structure in the Southern Hemisphere, with a notable positive center over the south Pacific and a downstream negative center over the SA continent. They behave slightly stronger at 500 hPa. Correspondingly, there is a low SLP anomaly central in the south Pacific

indicating the weaker-than-normal south Pacific subtropical high. Accompanied with this low SLP center, northwestern wind anomalies from the south Pacific arrive at the SA continent between the latitudes 45°S – 40°S . While due to the negative climatological temperature gradients, this flow causes cold advection as we discussed in last section. Meanwhile, a branch of northerly wind can arrive at the latitude 40°S from the north SA (Figs. 5e, 2a). As above discussed, it is critical to the warm center in the positive EOF1 mode. However, it fails to be explained by the horizontal circulation anomalies. We will expand on this point in terms of a regional Hadley cell later.

Associated with the EOF2 mode, an extratropical barotropic wave train pattern is distinctly observed in the streamfunction anomalies at different levels (Fig. 5b, d, f). This wave train pattern has positive and negative anomalies at interval arcing across the ocean between the Australian continent and the SA continent. This wave train is amplified over the Bellingshausen Sea, at where it displays a remarkable enhanced low pressure. This robust low-pressure anomaly brings strong westerly wind to the southern tip of the SA continent, which contributes the warm temperature advection in Fig. 2b. Prevailing wind anomaly over the southeast Brazil is southeasterly. It is related to the reflected part of the wave train, and contributes to the cold temperature advection over this region.

Barotropic wave train circulation patterns have been observed in different seasons in the southern extra-tropics, especially in the South Pacific–South America section (e.g. Karoly 1989; Berbery and Nogués-Paegle 1993; Mo and Paegle 2001; Garreaud et al. 2013; Müller and Berri 2007). It has been suggested that these patterns are closely connected with the rainfall and temperature variability in the SA continent (e.g. Díaz and Aceituno 2003; Cerne and Vera 2011; Berman et al. 2012). Jacques-Coper and Bronnimann (2014) reported a teleconnection from eastern Australia to southern SA over the South Pacific, associated with the summer-to-summer SAT variability (their Fig. 3a). Compared with their results, the wave train pattern detailed in this study is distinct because: (1) it is related to tropical streamfunction anomalies to the north of Australia; (2) the Oceania center here is located between 120°E–170°E, while in their work it is located farther east at 160°E; and (3) the strongest signal in the present study is over the Bellingshausen Sea, rather than over the Ross Sea. Hence, the dynamical details of subtropical barotropic

wave train patterns in different studies are possibly modulated by the differences in forcing and basic states.

3.3.2 Linkages with tropical SSTA and dynamics

Regional circulation anomalies are related to the global-scale teleconnections through the atmospheric bridge (Lau and Nath 1996; Trenberth et al. 1998; Alexander et al. 2002; Liu and Alexander 2007). Interannual variability in tropical SSTA is an important modulator in SA climate variability as reviewed. Warm and cold SSTA may result in local convection and precipitation change, and subsequent changes the divergence and convergence in atmosphere. Sequentially, the large scale zonal and meridional cells and the zonal asymmetric circulations may be changed through thermal wind adjustment and Rossby wave energy dispersion. To clarify the linkages between the tropical SSTA and the EOFs, Fig. 6 shows the correlation map between the SSTA and corresponding PCs. It shows the EOF1 is closely related to the warm SSTA in tropical eastern Pacific, south Pacific and south Atlantic, and the cold SSTA in tropical western Pacific. This SSTA pattern is similar to the classical El Niño pattern, in agreement with Barros et al. (2002). The correlation coefficient between the PC1 and the Niño 3.4 index is about 0.5 significant at 99% confidence level.

Corresponding to the El Niño-like SSTA pattern, rainfall is reduced in the Maritime Continent and enhanced in the equatorial central Pacific (Fig. 7a). Associated velocity potential displays a zonal wavenumber 1 pattern, with divergence over the central Pacific and convergence over the tropical Indian Ocean and the northwest SA. Vertical circulation averaged over 10°S–10°N (Fig. 8a) shows ascent anomalies over the central Pacific and descent anomalies over the Indian Ocean and the northwest SA. The sinking movement over the northwest SA further connects to

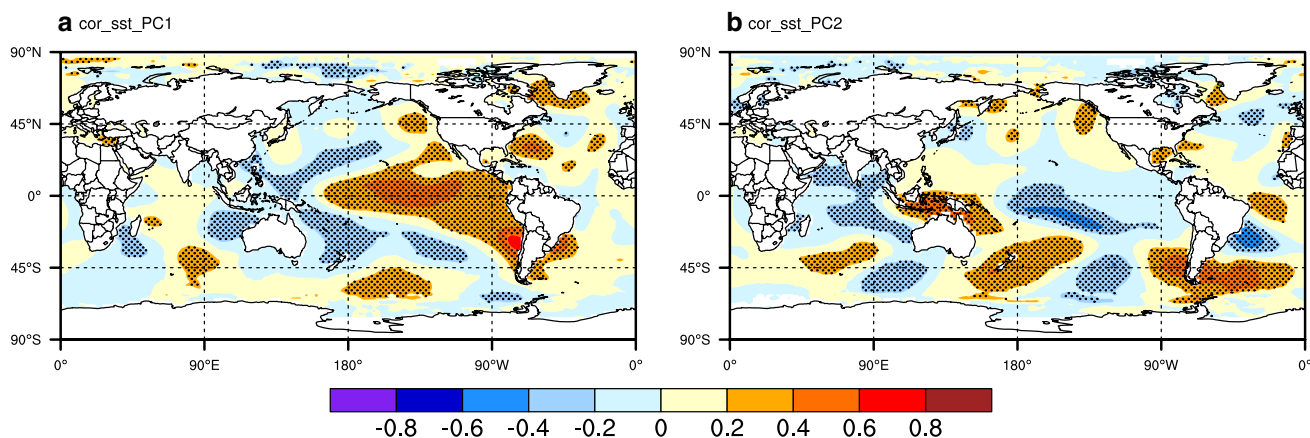


Fig. 6 Correlation maps between global SSTA and PCs. Stippling indicates their relationship significant at the 90% confidence level according to the two-tailed Student's t-test

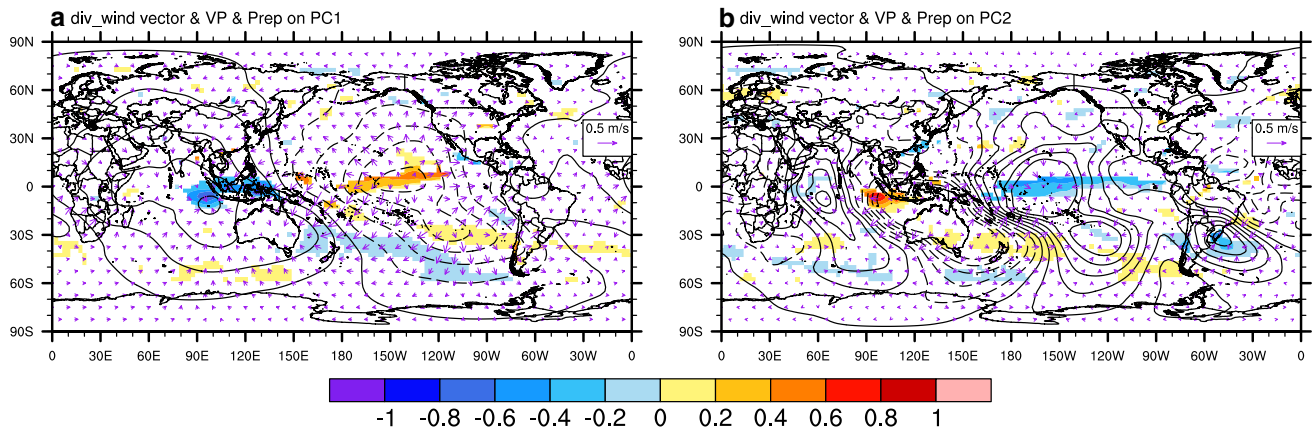


Fig. 7 Anomalies in divergent wind (arrows, unit: m s^{-1}), velocity potential (contours, unit: $10^5 \text{ m}^2 \text{ s}^{-1}$), and precipitation (shading, unit: mm day^{-1}) regressed onto the normalized PC1 and PC2. Precipitation

anomalies are shown at areas where they are significantly different from zero at the 90% confidence level according to the two-tailed Student's t-test

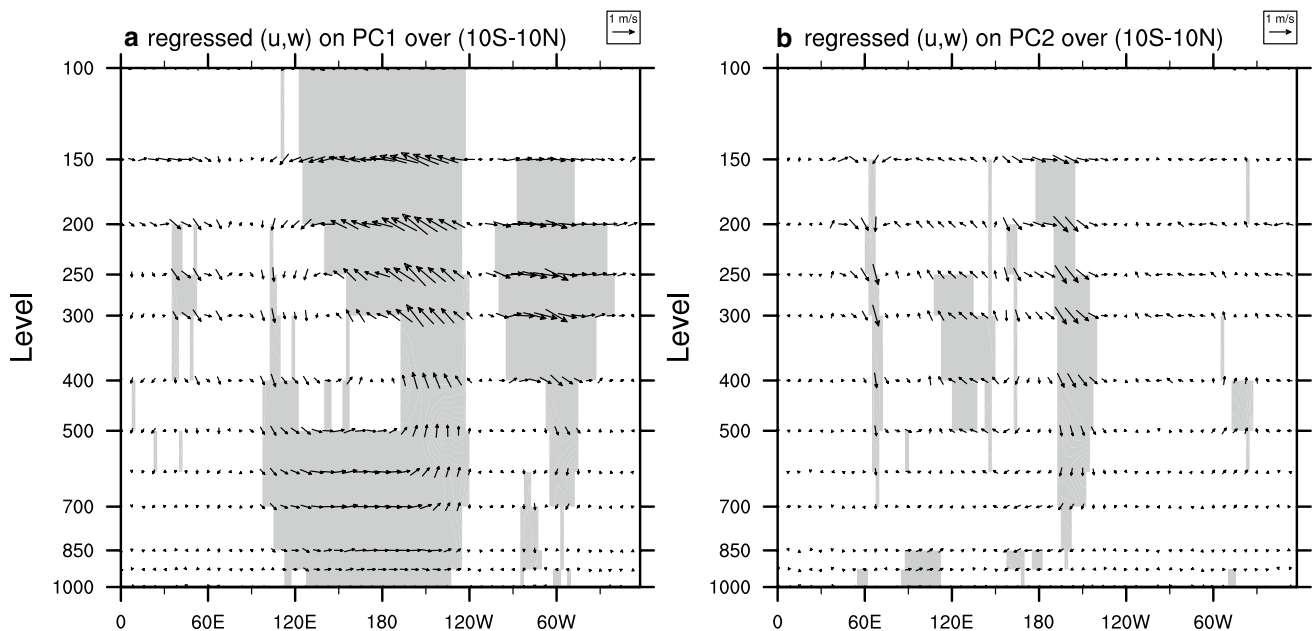


Fig. 8 Anomalies in zonal and vertical velocity (unit: m s^{-1}) regressed onto the normalized PC1 (a) and PC2 (b) averaged over (10°S–10°N) in the longitude-level section. Shading indicates either component of the vector significantly different from zero at the 90%

confidence level according to the two-tailed Student's test. Reference magnitude and length of vectors is indicated in the right top. Vertical velocity is multiplied by 1000

the significant ascent over the central SA (45°S–30°S), representing a regional Hadley cell over the longitudes 280°E–310°E (Fig. 9a). The northerly wind at the low levels as a branch of the Hadley cell is critical for the warm center in the positive EOF1. Besides, the ascent motion over the central SA may favor the increase in cloud cover and cause the SAT warming in this region via the cloud-radiation effect as discussed in Fig. 3.

For the EOF2, the SSTA displays a spatial pattern similar to the wave train in circulation (Fig. 6b). In the tropics,

remarkable warm SSTA appear in the surrounding oceans of the Maritime Continent, and cold anomalies appear in the tropical Indian ocean and middle–eastern tropical Pacific. These anomalies locate slightly at the south of the equator. Warm sea waters in the south Pacific and south Atlantic surround the southern SA. Cold sea waters appear to the east of Brazil coastline. It suggests that the north–south SAT fluctuation in the EOF2 mode might change in conjunction with the nearby SSTA and be remotely related to tropical SSTA.

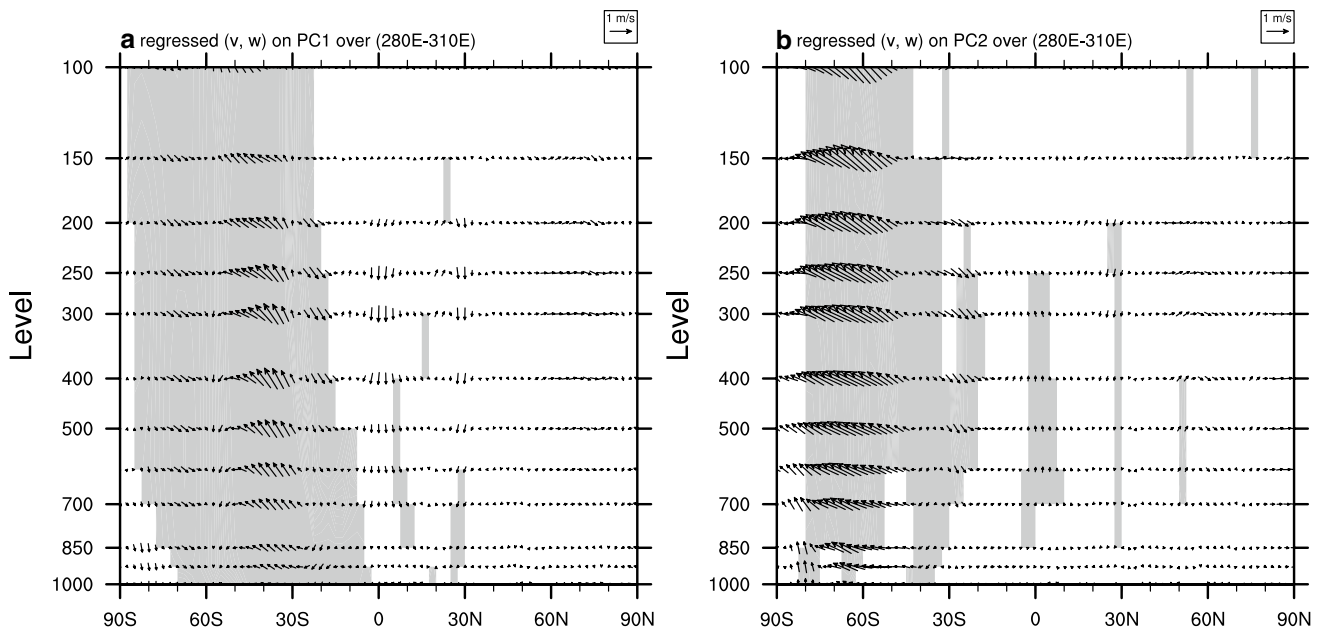


Fig. 9 Anomalies in meridional and vertical velocity (unit: m s^{-1}) regressed onto the normalized PC1 (a) and PC2 (b) averaged over (280°E–310°E) in the latitude-level section. Shading indicates either component of the vector significantly different from zero at the 90%

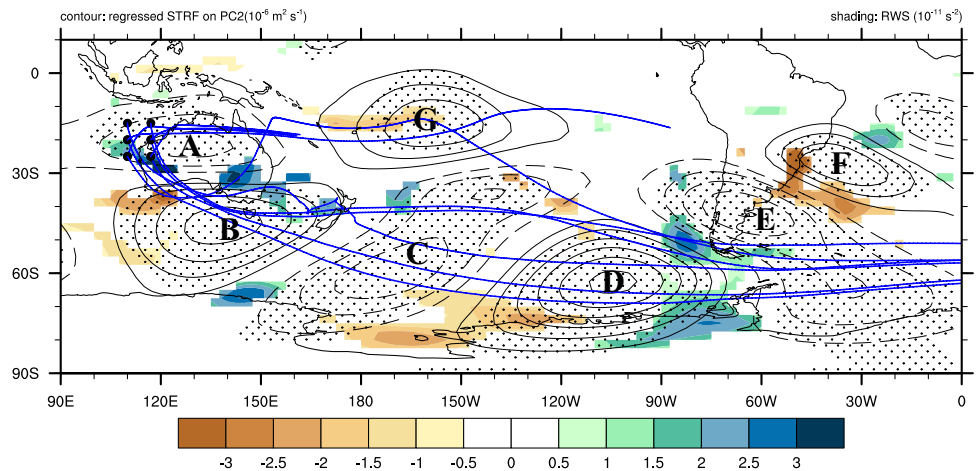
confidence level according to the two-tailed Student’s test. Reference magnitude and length of vectors is indicated in the right top. Vertical velocity is multiplied by 1000

Associated with the positive EOF2, more rainfall in the east equatorial Indian Ocean and less rainfall in the central equatorial Pacific and southwestern Atlantic are observed (Fig. 7b). The velocity potential field displays a zonal wave-number 2 pattern, and is much stronger in the southern subtropical zone. Unlike the EOF1, zonal tropical circulation changes insignificantly (Fig. 8b). Latitude-level circulation (Fig. 9b) shows descent and ascent flow at the latitudes of the southeast Brazil and the southern tip respectively. These vertical movements are consistent with the cloud cover changes in the corresponding regions. Considering the EOF2 is attributed to the horizontal advection at a large extent, it

is essential to check whether and how the quasi-barotropic wave train pattern in Fig. 5 links the tropical SSTA to the EOF2 mode.

Figure 10 shows the changes in the RWS at 200 hPa associated with the EOF2 and the Rossby wave trajectories starting from the north Australia. Details of the calculation were given in Sect. 2.3. We have set starting points over the area (110°–140°E, 30°S–15°S) on a grid 5° × 5°. Most ray paths exhibit similar trajectories. Therefore, only six points at the latitudes 25°S, 20°S and 15°S on the longitudes 110°E and 120°E are kept to show the trajectories clearer. There are two branches of wave rays initiated from the points at the

Fig. 10 Anomalies in Rossby wave source (shading, unit: 10^{-11} s^{-2}) and eddy streamfunction (contours, unit: $10^6 \text{ m}^2 \text{ s}^{-1}$) at 200 hPa regressed on the normalized PC2. Rossby wave ray paths starting from the black points are shown as blue curves indicating horizontal energy transmission by Rossby waves. Letters A–G indicate the negative and positive streamfunction centers



latitudes 20°S and 25°S, which indicate two waves capable in propagating meridionally with the initial zonal wavenumber 3. Rays are terminated when the total wavenumber exceeds 40 (corresponding to the length less than 1000 km).

To aid our description of Fig. 10, the notable seven streamfunction centers in the wave train are labeled as A–G. We can see that changes in the eddy streamfunction (centers A–G) are always accompanied by changes in the RWS over the same regions or vicinity. For centers A and G, RWS changes at the same location. Positive (negative) RWS anomalies favor the generation of positive (negative) vorticity and a negative (positive) streamfunction at center A (G). For the other centers, RWS generally changes at their upstream. Equation (1) shows that both the generation of vorticity from the RWS and its propagation (actually advection of vorticity by background wind) are important processes for changes in local rotational flow. Combining with the SSTA and divergent signals, we deduce that centers A and G mainly result from the RWS, and then their energy is transported downstream, which tend to displace the downstream RWS-generated vorticities. This inference is supported by the plotted wave ray pathways. Two trajectories string the individual centers into an integrated pattern. One is eastward propagation from A to G and then poleward to the southern SA. The other one is the typical great circle path, eastward and poleward across Australia and the Southern Ocean to the Bellingshausen Sea, and then equatorward to the south Atlantic.

3.3.3 AGCM simulation results

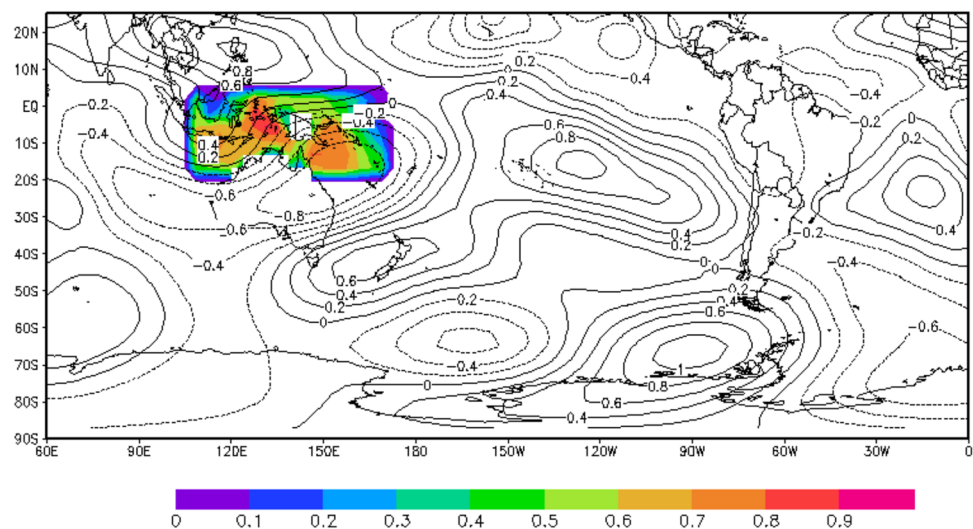
To further verify whether the warm and cold SSTA in the surrounding oceans of the Maritime Continent can trigger a wave train circulation pattern, two sets of the idealized numerical experiments are carried out by SPEEDY model.

The idealized positive SSTA is derived by regressing the SSTA in the region (110°–170°E, 20°S–0°) onto its area-averaged time series during the JJA season. The negative SSTA is simply set to be the opposite of the positive SSTA in order to avoid the nonlinear effect induced by the asymmetric SSTA pattern in different phases (Kucharski et al. 2006). The model is integrated over 768 months, and then the difference in the output climatological JJA streamfunction (with the zonal mean removed) between the positive and negative SSTA experiments is calculated to reflect the linear response to the prescribed SSTA (Fig. 11). Seven positive and negative centers in the observed wave train pattern are clearly identified in the simulated results, with the strongest one over the Bellingshausen Sea. However, there are also discrepancies between the simulation and the observation. For example, the circulation anomalies over the central-southern SA (center E in Fig. 10) in the simulation is dramatically weaker than the observation. At the same time, anomaly over the tropical eastern Pacific (center G in Fig. 10) is relatively stronger in the simulation than in the observation. Generally, the AGCM simulation suggest that the SSTA in the surrounding oceans of the Maritime Continent can excite a wave train pattern in circulation which transmit the wave energy to the SA and south Atlantic section.

4 Conclusions and discussion

This study examined the dominant modes of the austral winter SAT interannual variability in the SA continent during 1948–2014. The two leading EOF modes are characterized by remarkable anomalies in the central SA (EOF1) and a north–south dipolar fluctuation (EOF2). The EOF results are consistent with previous studies. Two distinct pathways

Fig. 11 Differences in the idealized SSTA (shading, unit: K) and 200 hPa eddy streamfunction (contours, unit: $10^6 \text{ m}^2 \text{ s}^{-1}$) between the warm and cold SSTA forcing experiments using the SPEEDY model



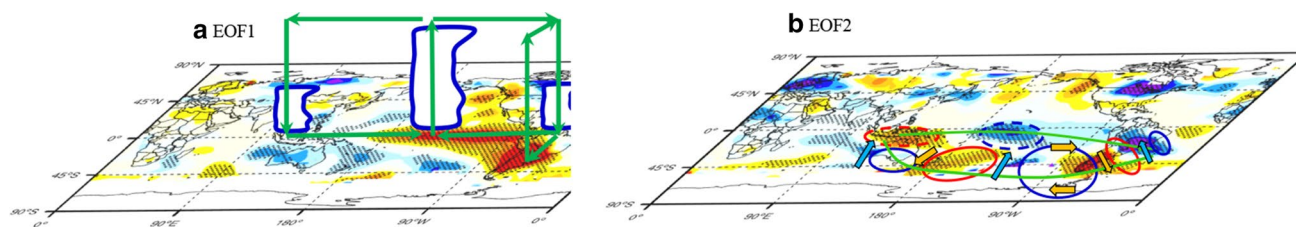


Fig. 12 Schematics showing the teleconnection from tropics to the SA associated with **a** the EOF1 and **b** the EOF2 modes. Background map shows the surface temperature regressed onto the normalized (a) PC1 and (b) PC2. Dashed contours in (b) indicate the tropical baro-

clinic circulation anomalies at upper levels, and solid contours indicate the barotropic wave train. Red and blue contours indicate the positive and negative streamfunction anomalies. Green curves in (b) indicate wave ray trajectories starting from the northern Australian

of the atmospheric bridge are involved in linking the remote tropical SSTA and the EOFs. For the EOF1, the El Niño type SSTA is accompanied by enhanced Walker circulation, which strengthens the downward branch in the north SA and then relates to a regional Hadley cell over the SA longitudes. The low-level branch of this meridional cell is northerly flow, which favors the warm advection in the central SA. These processes are summarized in Fig. 12a. The associated cloud-radiation effect is also discussed. It plays an opposite role to the temperature advection in the latitudes 45°S–30°S and north of 5°S, which results in insignificant SAT changes in these regions.

For the EOF2, the SSTA in the surrounding oceans of the Maritime Continent can excite a quasi-barotropic wave train which propagates as two-dimensional Rossby waves away from the forcing to the SA continent and south Atlantic via two trajectories. This mechanism is summarized in Fig. 12b. This barotropic wave train plays an important role in modulating the north–south SAT fluctuation by impacting the low-level temperature advection. Warm advection by the westerly wind from the south Pacific and the increased cloud cover induced by robust vertical motion together contribute the significant warm anomalies in the southern tip of the SA continent. Oppositely, cold advection by the southeast wind from the Atlantic is the primary factor of the cooling southeast Brazil. The decreased cloud cover plays as a secondary factor by reflecting less-than-normal outgoing longwave fluxes to the surface.

In this study, several findings in previous studies have been reproduced, including the effect of the tropical eastern SSTA, and the north–south SAT fluctuation between the southeast Brazil and the southern tip of the continent. Advancements are presented in the following aspects. Firstly, the winter-to-winter SAT variability in the whole SA continent is deliberated. Secondly, the impacts of tropical SSTA in the eastern Pacific and surrounding Maritime Continent are suggested as remote modulators on the EOF1 and EOF2 via different atmospheric bridge mechanisms. At last, associated cloud-radiation and advection processes for subregional SAT anomalies are discussed.

Since the time period discussed here covers the pre-satellite time when the quality of reanalysis data may be questionable, we plotted figures for the 1979–2014. They are similar to those presented here. The uncertainty in the quality of the cloud and radiation fluxes data from NCEP is examined by comparing with the ERA40 data. Results are generally consistent, especially in the concerned areas. However, further studies are still worthy, such as effect of more deliberated cloud-radiation processes and surface covering on SAT changes.

Teleconnection from tropical forcing, including SSTA in the tropical eastern Pacific and tropical Atlantic, and convection systems associated with the Madden–Julian Oscillation (MJO), play important roles in modulating climate variability over South America on multiple time-scales (Moura and Shukla 1981; Kiladis and Weickmann 1997; Bombardi et al. 2014; Shimizu and Ambrizzi 2016). For the discussed north–south SAT dipole, the SSTA in the surrounding oceans of the Maritime Continent is an important modulator by exciting a quasi-barotropic wave train in atmosphere. The importance of the barotropic wave train on climate variabilities in the SA is in agreement with previous studies (e.g. Karoly 1989; Berbery and Nogués-Paegle 1993; Mo and Ghil 1987; Mo and Higgins 1998; Mo and Paegle 2001; Carleton 2003; Garreaud et al. 2013; Müller and Berri 2007). However, the SSTA variability in this region has not been understood clearly. Simultaneous relationships between the SAT and SSTA are examined in this study. The lead-lag relationships between them need further studies. Besides, the decadal variability and its interaction with the interannual variability are also important topics.

Acknowledgements The authors thank two anonymous reviewers for providing useful comments. This work was jointly supported by the National Natural Science Foundation of China (NSFC) (projects 41575060 and 91437216), the SOA International Cooperation Program on Global Change and Air-Sea Interactions (GASI-IPOVAI-03). NCEP/NCAR reanalysis data, PREC precipitation data, and ERSST V4 data are provided by the NOAA/OAR/ESRL PSD, Boulder, Colorado, USA, from their Web site at <http://www.esrl.noaa.gov/psd/>.

References

- Aceituno P (1988) On the functioning of the Southern Oscillation in the South American sector. Part I: surface climate. *Mon Weather Rev* 116:505–524
- Alexander MA, Bladé I, Newman M et al (2002) The atmospheric bridge: The influence of ENSO teleconnections on air-sea interaction over the global oceans. *J Clim* 15:2205–2231
- Barreiro M, Tippmann A (2008) Atlantic modulation of El Niño influence on summertime rainfall over Southeastern South America. *Geophys Res Lett* 35:L16704. <https://doi.org/10.1029/2008GL035019>
- Barros VR, Grimm AM, Doyle ME (2002) Relationship between temperature and circulation in Southeastern South America and its influence from El Niño and La Niña events. *J Meteorol Soc Japan* 80:21–32. <https://doi.org/10.2151/jmsj.80.21>
- Berbery EH, Nogués-Paegle J (1993) Intraseasonal interactions between the tropics and extratropics in the Southern Hemisphere. *J Atmos Sci* 50:1950–1965
- Berman AL, Silvestri G, Compagnucci R (2012) Eastern Patagonia seasonal precipitation: influence of southern hemisphere circulation and links with subtropical South American precipitation. *J Clim* 25:6781–6795. <https://doi.org/10.1175/JCLI-D-11-00514.1>
- Berman AL, Silvestri G, Compagnucci R (2013) On the variability of seasonal temperature in southern South America. *Clim Dyn* 40:1863–1878. <https://doi.org/10.1007/s00382-012-1596-5>
- Bombardi RJ, Carvalho LMV, Jones C, Reboita MS (2014) Precipitation over eastern South America and the South Atlantic Sea surface temperature during neutral ENSO periods. *Clim Dyn* 42:1553–1568. <https://doi.org/10.1007/s00382-013-1832-7>
- Bracco A, Kucharski F, Kallummal R, Molteni F (2004) Internal variability, external forcing and climate trends in multi-decadal AGCM ensembles. *Clim Dyn* 23:659–678
- Carleton AM (2003) Atmospheric teleconnections involving the Southern Ocean. *J Geophys Res* <https://doi.org/10.1029/2000jc000379>
- Cerne SB, Vera CS (2011) Influence of the intraseasonal variability on heat waves in subtropical South America. *Clim Dyn* 36:2265–2277. <https://doi.org/10.1007/s00382-010-0812-4>
- Chen M, Xie P, Janowiak JE, Arkin PA (2002) Global Land Precipitation: A 50-yr Monthly Analysis Based on Gauge Observations. *J of Hydrometeorology* 3:249–266
- Chen SF, Wu RG, Liu Y (2016) Dominant modes of interannual variability in Eurasian surface air temperature during boreal spring. *J Clim* 29:1109–1125. <https://doi.org/10.1175/JCLI-D-15-0524.1>
- Collins JM, Chaves RR, da Silva Marques V (2009) Temperature variability over South America. *J Clim* 22:5854–5869. <https://doi.org/10.1175/2009JCLI2551.1>
- Coronato F, Bisigato A (1998) A temperature pattern classification in Patagonia. *Int J Climatol* 18:765–773
- Díaz A, Aceituno P (2003) Atmospheric circulation anomalies during episodes of enhanced and reduced convective cloudiness over Uruguay. *J Clim* 16:3171–3185
- Dogar MM, Kucharski F, Azharuddin S (2017) Study of the global and regional climatic impacts of ENSO magnitude using SPEEDY AGCM. *J Earth Syst Sci*. <https://doi.org/10.1007/s12040-017-0804-4>
- Garreaud RD (1999) Cold air incursions over subtropical and tropical South America: A numerical case study. *Mon Weather Rev* 127:2823–2853
- Garreaud RD (2000) Cold air incursions over subtropical South America: mean structure and dynamics. *Mon Weather Rev* 128:2544–2559
- Garreaud RD, Vuille M, Compagnucci R, Marengo J (2009) Present-day South American climate. *Palaeogeogr Palaeoclimatol Palaeoecol* 281:180–195. <https://doi.org/10.1016/j.palaeo.2007.10.032>
- Garreaud RD, Lopez P, Minvielle M, Rojas M (2013) Large-scale control on the Patagonian Climate. *J Clim* 26:215–230. <https://doi.org/10.1175/JCLI1200001.1>
- Grimm AM (2003) The El Niño impact on the summer monsoon in Brazil: regional processes versus remote influences. *J Clim* 16:263–280
- Grimm AM (2004) How do La Niña events disturb the summer monsoon system in Brazil? *Clim Dyn* 22:123–138
- Grimm AM (2011) Interannual climate variability in South America: Impacts on seasonal precipitation, extreme events, and possible effects of climate change. *Stoch Environ Res Risk Assess* 25:537–554. <https://doi.org/10.1007/s00477-010-0420-1>
- Grimm AM, Natori AA (2006) Climate change and interannual variability of precipitation in South America. *Geophys Res Lett* 33:1–5. <https://doi.org/10.1029/2006GL026821>
- Grimm AM, Zilli MT (2009) Interannual variability and seasonal evolution of summer monsoon rainfall in South America. *J Clim* 22:2257–2275. <https://doi.org/10.1175/2008JCLI2345.1>
- Halpert MS, Ropelewski CF (1992) Surface temperature patterns associated with the Southern Oscillation. *J Clim* 5:577–593
- Held IM, Suarez MJ (1994) A proposal for the intercomparison of dynamical cores of atmospheric general circulation models. *Bull Am Meteorol Soc* 75:1825–1830
- Herceg Bulic I, Brankovic C (2007) ENSO forcing of the Northern Hemisphere climate in a large ensemble of model simulations based on a very long SST record. *Clim Dyn* 28:231–254
- Hoskins BJ, Karoly DJ (1981) The steady linear response of a spherical atmosphere to thermal and orographic forcing. *J Atmos Sci* 38:1179–1196
- Jacques-Coper M, Bronnimann S (2014) Summer temperature in the eastern part of southern South America: its variability in the twentieth century and a teleconnection with Oceania. *Clim Dyn* 43:2111–2130. <https://doi.org/10.1007/s00382-013-2038-8>
- Kalnay E et al (1996) The NCEP/NCAR 40-year reanalysis project. *Bull Amer Meteor Soc* 77:437–471
- Karoly DJ (1983) Rossby wave propagation in a barotropic atmosphere. *Dyn Atmos Ocean* 7:111–125
- Karoly DJ (1989) Southern Hemisphere circulation features associated with El Niño–Southern Oscillation events. *J Clim* 2:1239–1252
- Kayano MT, Andreoli RV, de Souza RAF, Garcia SR (2017) Spatiotemporal variability modes of surface air temperature in South America during the 1951–2010 period: ENSO and non-ENSO components. *Int J Climatol*. <https://doi.org/10.1002/joc.4972>
- Kiladis G, Diaz HF (1989) Global climatic anomalies associated with extremes in the Southern Oscillation. *J Clim* 2:1069–1090
- Kiladis GN, Weickmann KM (1997) Horizontal structure and seasonality of large-scale circulations associated with submonthly tropical convection. *Mon Weather Rev* 125:1997–2013
- Kucharski F, Molteni F, Bracco A (2006) Decadal interactions between the western tropical Pacific and the North Atlantic Oscillation. *Clim Dyn* 26:79–91
- Kucharski F, Bracco A, Yoo JH, Molteni F (2007) Low-frequency variability of the Indian monsoon-ENSO relationship and the Tropical Atlantic: the “Weakening” of the 1980s and 1990s. *J Clim* 20:4255–4266
- Kucharski F, Bracco A, Yoo JH, Molteni F (2009) A Gill-Matsuno-type mechanism explains the Tropical Atlantic influence on African and Indian monsoon rainfall. *Q J R Meteorol Soc* 135:569–579
- Kucharski F, Kang IS, Farneti R, Feudale L (2011) Tropical Pacific response to 20th century Atlantic warming. *Geophys Res Lett* 38:L03702. <https://doi.org/10.1029/2010GL046248>
- Kucharski F, Molteni F, King MP, Farneti R, Kang I-S, Feudale L (2013) On the need of intermediate complexity general circulation models: a ‘SPEEDY’ example. *Bull Amer Meteor Soc* 94:25–30. <https://doi.org/10.1175/BAMS-D-11-00238.1>

- Lau N-C, Nath MJ (1996) The role of the “atmospheric bridge” in linking tropical Pacific ENSO events to extratropical SST anomalies. *J Clim* 9:2036–2057
- Li YJ, Li JP (2012) Propagation of planetary waves in the horizontal non-uniform basic flow (in Chinese). *Chin J Geophys* 55:361–371
- Li L, Nathan TR (1997) Effects of low-frequency tropical forcing on intraseasonal tropical-extratropical interactions. *J Atmos Sci* 54:332–346
- Li YJ, Li JP, Jin FF, Zhao S (2015) Interhemispheric propagation of stationary Rossby waves in a horizontally nonuniform background flow. *J Atmos Sci* 72:3233–3256. <https://doi.org/10.1175/JAS-D-14-0239.1>
- Liu ZY, Alexander M (2007) Atmospheric bridge, oceanic tunnel, and global climate teleconnections. *Rev Geophys* 45:1–34. <https://doi.org/10.1029/2005RG000172.1>. INTRODUCTION
- Losada T, Rodríguez-Fonseca B, Kucharski F (2012) Tropical influence on the summer Mediterranean climate. *Atmos Sci Lett* 13:36–42
- Marengo J, Rogers J (2001) Cold front and Polar Air Outbreaks in the Americas during: Modern climate assessments and impacts, and some Past climate evidences. In: Markgraf V (ed) Present and past inter-hemispheric climate linkages in the Americas and their societal effects. Academic Press, London, pp 31–51
- Marengo J, Cornejo A, Satymurty P, Nobre C, Sea W (1997) Cold surges in tropical and extratropical South America: The strong event in June 1994. *Mon Weather Rev* 125:2759–2786
- Mo KC, Ghil M (1987) Statistics and dynamics of persistent anomalies. *J Atmos Sci* 44:877–902
- Mo KC, Higgins RW (1998) The Pacific–South American modes and tropical convection during the Southern Hemisphere winter. *Mon Weather Rev* 126:1581–1596
- Mo KC, Paegle JN (2001) The Pacific–South American modes and their downstream effects. *Int J Climatol*. 21:1211–1229. <https://doi.org/10.1002/joc.685>
- Mohino E, Losada T (2015) Impacts of the Atlantic Equatorial Mode in a warmer climate. *Clim Dyn* 45:2255–2271. <https://doi.org/10.1007/s00382-015-2471-y>
- Molteni F (2003) Atmospheric simulations using a GCM with simplified physical parameterizations. I. Model climatology and variability in multi-decadal experiments. *Clim Dyn* 20:175–191
- Moura AD, Shukla J (1981) On the dynamics of droughts in Northeast Brazil: observations, theory and numerical experiments with a general circulation model. *J Atmos Sci* 38:2653–2675
- Müller GV, Berri GJ (2007) Atmospheric Circulation associated with persistent generalized frosts in central southern South America. *Mon Weather Rev* 135:1268–1289. <https://doi.org/10.1175/MWR3344.1>
- Nnamchi HC, Li J, Kang IS, Kucharski F (2013) Simulated impacts of the South Atlantic Ocean Dipole on summer precipitation at the Guinea Coast. *Clim Dyn* 41:677–694. <https://doi.org/10.1007/s00382-012-1629-0>
- North GR et al (1982) Sampling errors in the estimation of empirical orthogonal functions. *Mon Weather Rev* 110:699–706
- Pittock AB (1980) Patterns of climatic variation in Argentina and Chile - II. Temperature, 1931–60. *Mon Weather Rev* 108:1362–1369
- Rodríguez-Fonseca B, Polo I, García-Serrano J, Losada T, Mohino E, Mechoso CR, Kucharski F (2009) Are Atlantic Niños enhancing Pacific ENSO events in recent decades? *Geophys. Res Lett* 36:L20705. <https://doi.org/10.1029/2009GL040048>
- Rusticucci M (2012) Observed and simulated variability of extreme temperature events over South America. *Atmos Res* 106:1–17. <https://doi.org/10.1016/j.atmosres.2011.11.001>
- Rusticucci M, Vargas W (1995) Synoptic situations related to spells of extreme temperatures over Argentina. *Meteor Appl* 2:291–300
- Sardeshmukh PD, Hoskins BJ (1988) The generation of global rotational flow by steady idealized tropical divergence. *J Atmos Sci* 45:1228–1251
- Schultz D, Bracken WE, Bosart L (1998) Planetary- and synoptic-scale signature associated with Central American cold surges. *Mon Weather Rev* 126:5–27
- Shimizu MH, Ambrizzi T (2016) MJO influence on ENSO effects in precipitation and temperature over South America. *Theor Appl Climatol* 124:291–301. <https://doi.org/10.1007/s00704-015-1421-2>
- Skansi M, Brunet M, Sigró J et al (2013) Warming and wetting signals emerging from analysis of changes in climate extreme indices over South America. *Glob Planet Change* 100:295–307. <https://doi.org/10.1016/j.gloplacha.2012.11.004>
- Storch HV, Zwiers FW (2003) Statistical analysis in climate research. Cambridge University Press
- Sun C, Li J, Jin FF (2015) A delayed oscillator model for the quasi-periodic multidecadal variability of the NAO. *Clim Dyn* 45:2083–2099. <https://doi.org/10.1007/s00382-014-2459-z>
- Torres RR, Marengo JA (2014) Climate change hotspots over South America: From CMIP3 to CMIP5 multi-model datasets. *Theor Appl Climatol* 117:579–587. <https://doi.org/10.1007/s00704-013-1030-x>
- Trenberth KE, Branstator GW, Karoly D et al (1998) Progress during TOGA in understanding and modeling global teleconnections associated with tropical sea surface temperatures. *J Geophys Res* 103:14291–14324
- Vera CS, Vigiariolo PK (2000) A diagnostic study of cold-air outbreaks over South America. *Mon Weather Rev* 128:3–24
- Vincent LA, Peterson TC, Barros VR et al (2005) Observed trends in indices of daily temperature extremes in South America 1960–2000. *J Clim* 18:5011–5023. <https://doi.org/10.1175/JCLI3589.1>
- Willmott CJ, Matsuura K (2001) Terrestrial air temperature and precipitation: monthly and annual time series (1950–1999), http://climate.geog.udel.edu/~climate/html_pages/README.ghcn_ts2.html
- World Meteorological Organization (2008) WMO statement on the status of the global climate in 2007. Switzerland
- World Meteorological Organization (2010) WMO statement on the status of the global climate in 2009. Switzerland
- World Meteorological Organization (2014) WMO statement on the status of the global climate in 2013. Switzerland
- Yadav RK, Yoo JH, Kucharski F, Abid MA (2010) Why is ENSO influencing Northwest India winter precipitation in recent decades? *J Clim* 23:1979–1993
- Zamboni L, Kucharski F, Mechoso CR (2012) Seasonal variations of the links between the interannual variability of South America and the South Pacific. *Clim Dyn* 38:2115–2129. <https://doi.org/10.1007/s00382-011-1116-z>
- Zhao S, Li JP, Li YJ (2015) Dynamics of an interhemispheric teleconnection across the critical latitude through a southerly duct during boreal winter. *J Clim* 28:7437–7456. <https://doi.org/10.1175/JCLI-D-14-00425.1>
- Zhou J, Lau KM (2001) Principal modes of interannual and decadal variability of summer rainfall over South America. *Int J Climatol* 21:1623–1644. <https://doi.org/10.1002/joc.700>